Chemical vapor deposition and high-resolution patterning of a highly conductive two-dimensional coordination polymer film

Víctor Rubio-Giménez,[1,*] Giel Arnauts,[1] Mingchao Wang,[2] Eduardo Sergio Oliveros Mata,[3] Xing Huang,[2] Tianshu Lan,[2] Max L. Tietze,[1] Dmitry E. Kravchenko,[1] Jorid Smets,[1] Nathalie Wauteraerts,[1] Azat Khadiev,[4] Dmitri V. Novikov,[4] Denys Makarov,[3] Renhao Dong,[2] and Rob Ameloot[1,*]

[1] Centre for Membrane Separations, Adsorption, Catalysis and Spectroscopy (cMACS), Katholieke Universiteit Leuven, Celestijnenlaan 200F, 3001 Leuven, Belgium

[2] Center for Advancing Electronics Dresden (cfaed) & Faculty of Chemistry and Food Chemistry, Technische Universität Dresden, 01062 Dresden, Germany

[3] Institute of Ion Beam Physics and Materials Research, Bautzner Landstrasse 400, 01328 Dresden, Germany

[4] Deutsches Elektronen-Synchrotron DESY, Notkestraße 85, 22607 Hamburg, Germany

ABSTRACT: Crystalline coordination polymers with high electrical conductivities and charge carrier mobilities might open new opportunities for electronic devices. However, current solvent-based synthesis methods hinder compatibility with microfabrication standards. Here, we describe a solvent-free chemical vapor deposition method to prepare high-quality films of the two dimensional conjugated coordination polymer Cu-BHT (BHT = benzenehexanothiolate). This approach involves the conversion of a metal oxide precursor into Cu-BHT nanofilms with a controllable thickness (20-85 nm) and low roughness (< 10 nm) through exposure to the vaporized organic linker. Moreover, the restricted metal ion mobility during the vapor-solid reaction enables high-resolution patterning via both bottom-up lithography, including the fabrication of micron-sized Hall bar and electrode patterns to accurately evaluate the conductivity and mobility values of the Cu-BHT films.

INTRODUCTION

Metal-organic graphene analogs (MOGs), are a novel subclass of layered materials that is gaining interest in electronics and magnetism.[1–4] These conductive materials consist of planar aromatic ligands and transition metal ions, resulting in conjugated hexagonal honeycomb, square, rhombic, or Kagome 2D lattices, thus including both porous metal-organic frameworks (MOFs) and non-porous coordination polymers (CPs). Their versatile electronic and magnetic properties, modulable by downsizing into the single- or few-layer regime,[5–7] have been used in a plethora of sensors,[8–10] field-effect transistors,[11,12] photodetectors,[13] spin vales,[14] solar cells[15], and even energy storage devices.[16]

Integration of MOGs into functional devices will require suitable processing methodologies. However, only a limited number of studies report the patterning of MOG films thus far, usually with poor resolution and pattern fidelity.[17,18] Additionally, robust thin film deposition methods are key in providing control over the material properties and ensuring standardization.[19,20] Yet, current solution-based methods to produce MOGs thin films lack control over nucleation and crystal growth, and the resulting coatings are typically rough and far from pinhole-free. Apart from particle contamination due to homogeneous nucleation, solution-based synthesis methods can lead to corrosion due to metal salts and surface-tension-related issues.[19] Chemical vapor deposition (CVD) of MOFs and CPs is a solvent-free methodology that avoids these problems by reacting a metal-containing precursor film with a ligand in the vapor phase to yield the desired material.[21,22] This technique was pioneered for zeolitic imidazolate frameworks (ZIFs)[23–30] and has since been extended to other MOFs and CPs.[31–39] The absence of solvent during this approach limits metal ion mobility during crystallization, enabling the conversion of patterned oxide precursors with high fidelity in bottom-up lithography procedures.[23,25,29] In contrast, solvent-based syntheses typically yield poorly defined edges,[2,19,40] leaving top-down patterning methodologies as the only option.[41,42]

Here, we report the CVD of Cu-BHT films (BHT = benzenehexanothiolate) using an oxide precursor layer. Cu-BHT is one of the few Kagome-type MOGs (**Figure 1a-c**) and is a metallic conductor with the highest conductivity reported in a metal-organic compound.[6,37,43] Thus far, this material has mainly been synthesized through interfacial liquid-liquid reactions yielding inhomogeneous and rough films. In contrast, the CVD Cu-BHT nanofilms reported here are homogeneous over large areas and smooth while maintaining the crystallinity, high electrical conductivity and charge carrier mobility. Moreover, the conversion from a CuO precursor layer allows for controlling the final Cu-BHT film thickness over a broad nanometric range (20-85 nm), and is fully compatible with additive lithography processes (e.g., lift-off patterning) with a resolution

down to the μm range. Microscale patterning is a fundamental step in microfabrication of electronic devices.[19]

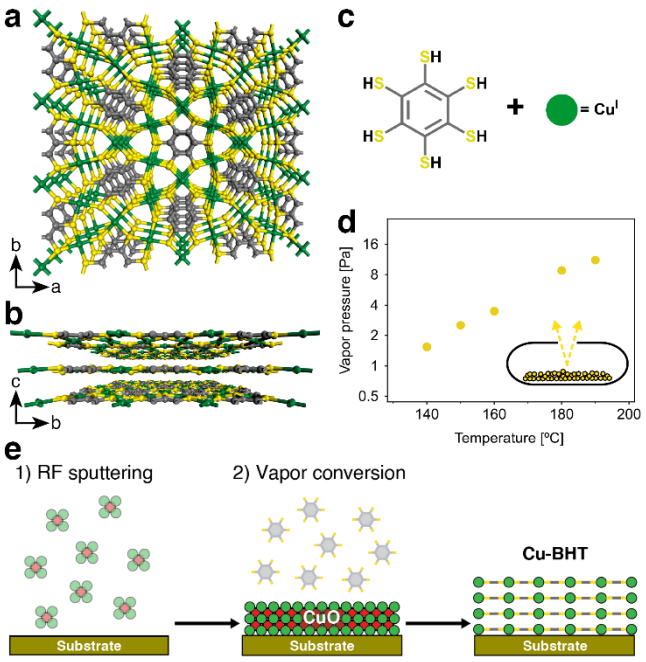

Figure 1. Cu-BHT structure and CVD procedure. a) Top view of the Cu-BHT crystal structure showing the Kagome-type planar lattice with the chemical formula $[Cu_3(C_6S_6)]_n$. Cu, C, and S atoms are colored green, grey, and yellow, respectively. b) Side-view of the eclipsed (AA) vertical stacking of the Cu-BHT layers. c) Building blocks of Cu-BHT: Cu^{I} ion and H_6BHT linker. d) Vapor pressure of the H_6BHT linker as a function of temperature as determined via Knudsen effusion cell measurements (scheme shown as inset). e) Scheme of the 2-step CVD procedure to prepare Cu-BHT nanofilms: a CuO layer is deposited via RF sputtering, followed by exposure to H_6BHT vapor.

RESULTS AND DISCUSSION

To assess the viability of the CVD route for Cu-BHT, the vapor pressure and stability of the BHT ligand was determined as a function of temperature using a Knudsen effusion cell (**Figure S1**) and thermogravimetric analysis (**Figure S2**). Since H_6BHT showed a sufficiently high vapor pressure of > 1 Pa at temperatures above 140 °C (**Figure 1d**), preliminary reactivity tests were carried out by sealing a mixture of CuO nanopowder (< 50 nm) and H_6BHT linker inside of a evacuated ampoule and heating it at 150 °C for 12 hours. Powder X-ray diffraction (PXRD) and scanning electron microscopy (SEM) measurements confirmed the successful formation of crystalline Cu-BHT under these conditions (**Figure S3 and S4**). Hence, for the fabrication of Cu-BHT nanofilms, we followed a two-step process as depicted in **Figure 1e**. First, a CuO layer was deposited via Ar plasma sputtering onto either a Si, Si/SiO_2 wafer or glass substrates. Spectroscopic ellipsometry was used to determine the exact thicknesses (**Figure S5**). Subsequently, this oxide precursor layer was converted into Cu-BHT through a vapor-solid reaction with the vaporized H_6BHT ligand. To this end, the CuO substrate and a boat with H_6BHT powder were loaded into separate areas of a multi-zone CVD furnace and heated under dynamic vacuum (ca. $4{\cdot}10^{-3}$ mbar) to 150 °C and 140 °C, respectively, by using precise temperature control with thermocouples near the substrate (**Figure S6**). The substrate was kept at a higher temperature than the ligand powder to avoid condensation of H_6BHT vapor. After 10 hours of exposure, the brown CuO layer converted into a uniform blue coating over large centimeter-scale areas (**Figure 2a**).

Atomic force microscopy (AFM) topography images of the film surface (**Figure 2b** and **Figure S7**), corroborate the formation of homogeneous and smooth coatings over micrometric-scale areas. The film thickness was assessed by AFM by analyzing physically scratched areas (**Figure 2c**). These measurements confirmed that, as with previous demonstrations of CVD of MOFs from metal oxide precursors,[23] the thickness of the final metal-organic film can be controlled via the precursor layer: the Cu-BHT thickness scales linearly with the initial CuO thickness, resulting in a consistent 7× expansion (**Figure 2d**). Remarkably, the root-mean-square (RMS) roughness only slightly increases with film thickness (5.7 ± 1.6 nm vs. 10.8 ± 1.7 nm for 20 nm and 85 nm films, respectively; **Figure S7-8**). These values are in line with those reported for MOF-CVD films and lower than for 2D MOG films obtained via solution-based methods (> 13 nm).[15,44,45]

The reciprocal space maps resulting from 2D grazing incidence X-ray diffraction (2D-GIXRD) (**Figure 2e**) demonstrate the formation of crystalline Cu-BHT (AA stacking; monoclinic, C2; a = 15.016 Å, b = 8.691 Å, c = 3.489 Å, β = 101.501).[6] The appearance of (h00), (0l0), and (hk0) diffractions uniquely in the in-plane direction, with the 001 reflection only appearing out-of-plane, indicates the preferential orientation of the Cu-BHT crystallites with their 2D ab planes parallel to the substrate (**Figure 2d-e**). This orientation is the same as obtained through liquid-liquid interfacial synthesis.[44] The absence of CuO peaks in 2D-GIXRD patterns for Cu-BHT films up to 85 nm (**Figure S9**) indicates the complete conversion of the precursor layer. However, a Cu-BHT thin film converted from a 40-nm thick CuO layer features the characteristic diffraction ring for polycrystalline CuO (**Figure S9**).

Hard X-ray photoelectron spectroscopy (HAXPES) was employed to determine the elemental composition and oxidation states of the Cu-BHT nanofilms. In HAXPES, hard X-rays (GaKα: 9.2 keV from a liquid Ga jet source) are used instead of conventional, lower-energy X-rays (e.g., AlKα: 1.5 keV) to produce photoelectrons with an inelastic mean free path that is several times larger.[46] Therefore, HAXPES provides information on the entire Cu-BHT film thickness.[30] Thus, the Si and O peaks from the substrate (*i.e.*, the native SiO_2 layer on top of the wafer) appear in the survey spectra of a 80-nm Cu-BHT film together with those of the elements in Cu-BHT (Cu, S, and C) (**Figure S10**). The Cu 2p spectra of the CVD Cu-BHT films (**Figure S11**) are near-identical to those for a reference sample prepared using the standard liquid-liquid synthesis, regardless of film thickness, indicating a complete conversion of the CuO precursor. The binding energies (BE) of 953.1 and 932.3 eV correspond to the Cu 2p 1/2 and 2p 3/2 regions, respectively. As shown in **Figure 2f**, the Cu 2p 3/2 region shows a main peak at 932.6 eV with a shoulder at higher BE and no significant satellite peaks, thus pointing to the exclusive presence of Cu^{I}, in line with previously reported X-ray photoelectron spectroscopy (XPS) measurements of Cu-BHT.[15,37,44,45,47] Since the sputtered starting material is

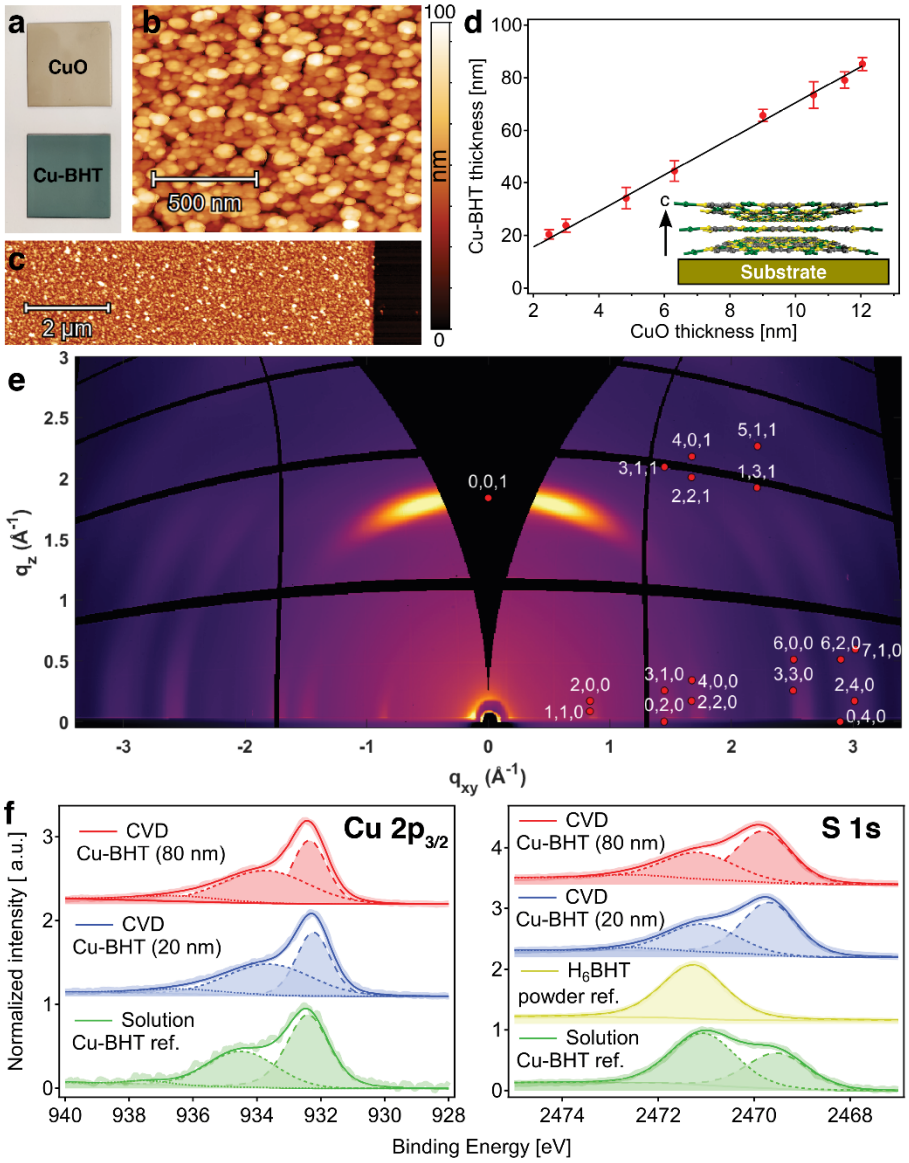

Figure 2. Physical characterization of CVD Cu-BHT nanofilms. a) Photograph of glass substrates (3x3 cm^2) with a 11-nm CuO layer before conversion (top) and a 80-nm CVD Cu-BHT film (bottom). b) AFM topographic image of a homogeneous 20 nm CVD Cu-BHT nanofilm and; c) a manually scratched area of the same film. d) CVD Cu-BHT film thicknesses obtained from CuO precursor films with different thicknesses. The linear fit of the data yielded an expansion factor of 7×. e) Synchrotron 2D-GIXRD reciprocal space map of a crystalline CVD Cu-BHT nanofilm (20 nm). Simulated positions of Bragg peaks for a (001) orientation are indicated with red dots and labeled in white. Inset in (d) shows this orientation of Cu-BHT with respect to the substrate and the crystallographic c axis. f) High-resolution HAXPES spectra of the Cu 2p 2/3 and S 1s regions of CVD Cu-BHT nanofilms and powder references of solution-made Cu-BHT and H_6BHT ligand

predominantly composed of CuO with a minor fraction of Cu^0 (**Figure S12**), the reduction of Cu^{II} to Cu^I must occur during the vapor-solid reaction with H_6BHT. Based on previous studies of Cu-thiolate self-assembled mono- and multilayers,[48,49] we hypothesize that first CuO can be reduced via the oxidation of the thiol groups in H_6BHT to disulfides, followed by the formation of Cu-thiolate bonds with the excess vaporized linkers. For the Cu^0 centers, Cu-BHT formation occurs via oxidative addition of the S–H bond followed by reductive elimination of hydrogen.[48] The S 1s region shows a maximum at 2470 eV and a broad shoulder at higher BE, which is consistent with the formation of Cu-thiolate bonds.[50,51] As specified in **Table S1**, the overall S/Cu ratio was calculated to be fairly close to the theoretical value of 2 as given by the chemical formula of $[Cu_3(C_6S_6)]$, regardless of film thickness. Since the asymmetric Cu 2p 3/2 and S 1s peaks in both the CVD nanofilms and the reference sample can be fitted to two (mixed Lorentz-Gaussian) subpeaks each, two different S chemical environments likely exist in both cases. This observation is in agreement with previously reported XPS measurements on Cu- BHT that also show a dominant Cu 2p 3/2 subpeak at lower BE and a smaller one at higher BE.[15,44,45,52,53] Likewise, the S 1s region has an intense subpeak at lower BE and a smaller high-BE shoulder. Comparison with the HAXPES S 1s spectra of the free H_6BHT ligand hints at the higher BE subpeak corresponding to uncoordinated S atoms or with a different oxidation state. We ascribe these higher BE subspecies to the existence of defective sites in the Cu-BHT nanocrystallites.[37,44,45]

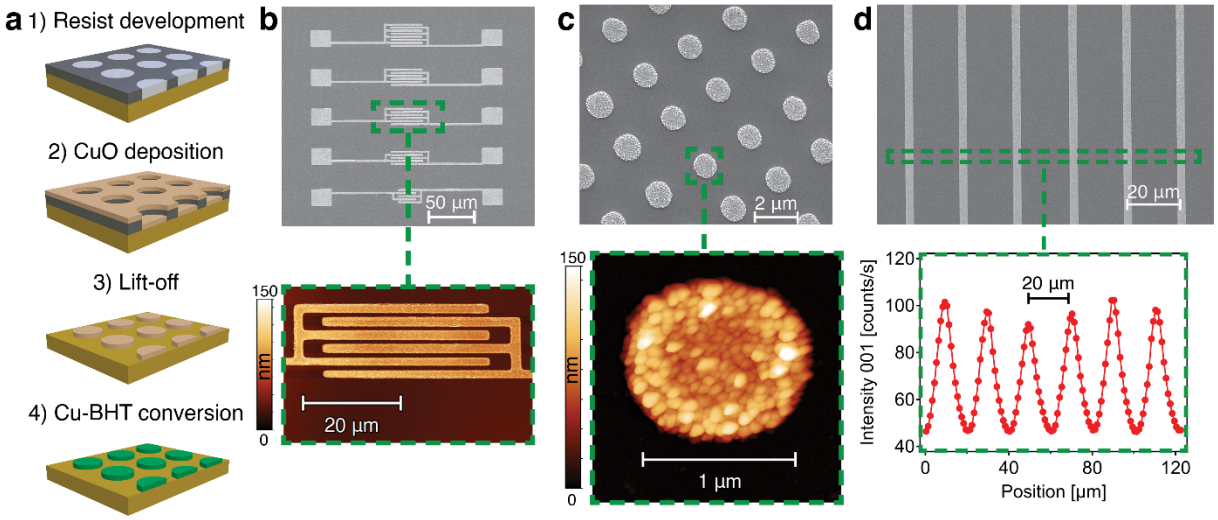

Figure 3. Bottom-up patterning of CVD Cu-BHT. a) Fabrication process combining bottom-up additive lithography and CVD. SEM image and AFM topography close-up of patterned Cu-BHT interdigitated electrodes (b) and circular features (c) fabricated this way. d) SEM image of line patterns of Cu-BHT fabricated this way (top) and synchrotron µ-XRD scanning of the pattern by displacing the microbeam across the lines (bottom). The extracted intensity of the 001 diffraction peak is plotted against the lateral position.

To showcase the versatility of the CVD methodology in patterning Cu-BHT films, we evaluated bottom-up additive lithography, commonly referred to as 'lift-off patterning'. In this approach, a blanket film of the target material is deposited on a substrate covered with a single-use mask, typically a patterned photoresist layer. The latter is subsequently removed with an organic solvent. While resist swelling and premature dissolution are potential problems in solvent-based syntheses, such issues are avoided in vapor-based methods.[23] Furthermore, in two-step CVD method, the resist can be removed either after CuO precursor deposition (**Figure 3a**) or after Cu-BHT formation. Hence, it is possible to completely avoid contact of the 2D MOG layer with any solvent to ensure the maintenance of its chemical and physical integrity. Additionally, it can facilitate integration in microfabrication, as patterning of oxides and metals can rely on well-established protocols.[19] Converting patterned CuO into Cu-BHT reproduces the patterns with high fidelity and resolution as confirmed via AFM, SEM and confocal microscopy. Amongst other patterns (see **Figure S13**), we fabricated interdigitated Cu-BHT electrodes with a minimum separation of 750 nm between the 2 µm wide fingers (**Figure 3b**). The minimum feature

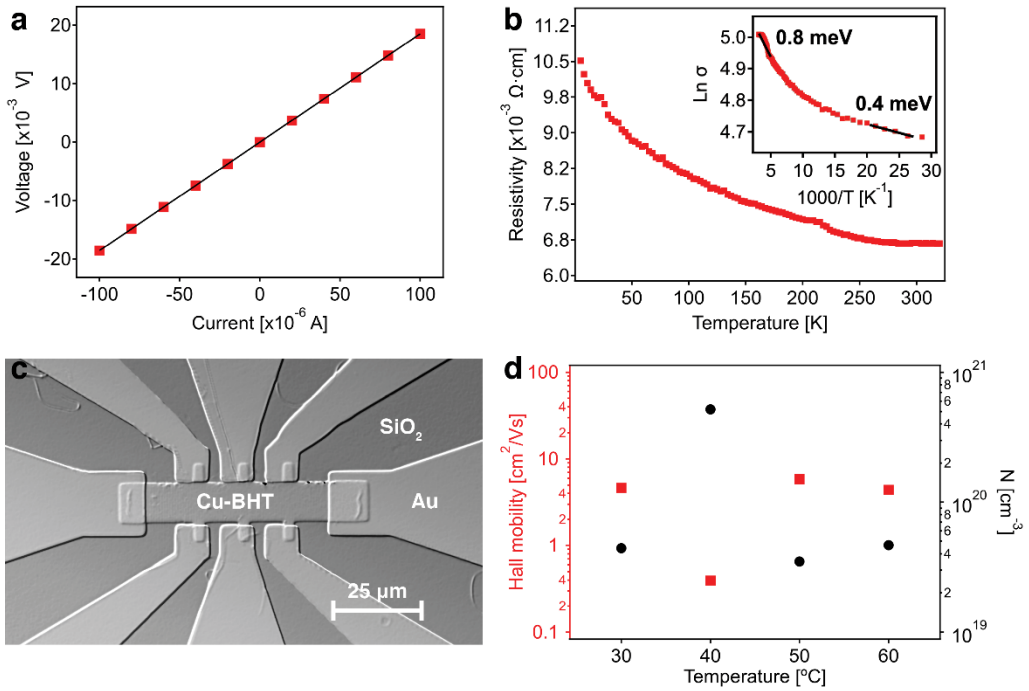

Figure 4. Electronic properties of CVD Cu-BHT devices. a) *I-V* curve of a 85-nm Cu-BHT film at 300 K. Black line is a linear fit of the data. b) Resistivity of a 85-nm film as a function of temperature (T) ranging from 2 to 320 K measured with the van der Pauw geometry. Inset shows the plots of ln σ versus 1000/T with Arrhenius fits for the activation energies. c) Confocal microscopy image of a Hall bar microdevice (Cu-BHT Hall bar and Au electrodes) made with additive lithography. d) Hall charge mobility and charge carrier density versus temperature obtained from Hall effect measurements.

size achievable through this methodology were circles of 500 nm radius (**Figure 3c**). The crystallinity of the patterned features was confirmed for 3 μm lines spaced 20 μm apart (**Figure 3d top**) through synchrotron micro-XRD (μ-XRD) in grazing-incidence mode, by scanning across a 3.5 μm X-ray microbeam. No diffraction was visible in between the lines, whilst the lines themselves yielded the characteristic Cu-BHT pattern (**Figure S14**). The extracted intensity of the 001 peak *vs.* the lateral position confirmed the 20 μm separation between the crystalline Cu-BHT lines (**Figure 3d bottom)**.

Next, we compared lift-off patterning with plasma etching lithography, an alternative, top-down method to pattern solution-made MOF films.[17,18] In the latter case, a single-use photoresist mask is deposited and patterned on top of the MOF layer. Subsequently, the patterned is transferred into the MOF layer by plasma etching, and the remaining resist is removed (**Figure S15a**). In this approach, the MOF must withstand not only the deposition and removal of the resist but also the plasma etching step. Inspection of 3 μm Cu-BHT lines spaced 20 μm apart fabricated this way revealed damage at the line edges previously covered by the resist (**Figure S16**). Furthermore, a synchrotron μ-XRD line scan revealed that Cu-BHT removal in between the lines was not complete, as the characteristic 001 peak remained observable (**Figure S15b-c**). Moreover, as visible in **Figures S14 and S15**, the 001 peak resulting from the Cu-BHT lines is more defined and intense for patterns obtained through lift-off in comparison to Ar plasma etching, due to damage during the latter process.

Finally, we explored the electronic properties of the CVD Cu-BHT nanofilms with different thicknesses (20-85 nm) by performing temperature-dependent resistance measurements in the van der Pauw configuration. The linear current-voltage (*I*–*V*) curves ensure Ohmic contacts (**Figures 4a and S17**) and yield conductivity (σ) values at 300 K ranging from 342 S/cm for a 20-nm film to 634 S/cm for a 85-nm one, in line with films of similar thickness prepared by liquid-liquid interfacial synthesis and measured using the standard four-probe method.[44] By decreasing the temperature from 320 to 2 K, the 85-nm film displays a slow increase of resistance (**Figure 4b**). The relationship between ln σ and the reciprocal of the device temperature (inset, **Figure 4b**) is nonlinear, as previously reported for substantially thicker Cu-BHT films and commonly observed for other highly conducting coordination polymers.[54] As shown in **Figure S18**, Arrhenius fits yield activation energies (E_a) of 0.8 and 0.4 meV for the high (300 K) and low (40 K) temperature regions, respectively. In the 80-220 K range, the transport regime can be fitted to a Mott's 3D variable range hopping model, as ln σ follows a $T^{-1/4}$ dependence (**Figure S19**). The transparency of the films was subsequently evaluated with ultraviolet-visible-near infrared (UV-Vis-NIR) spectroscopy. As visible in **Figure S20**, the transmittance drops by almost half for a 85-nm film with respect to the glass substrate, but it barely changes by 8% for a 20-nm film, thus confirming the potential of Cu-BHT as a transparent electrode.[15,44]

In an effort to further analyze the charge transport properties of our CVD nanofilms, we took advantage of the compatibility of our method with additive lithography and fabricated Hall bar microdevices with a minimum feature size of 2 μm (Hall arms width, **Figure 4c**). Hall effect measurements of Cu-BHT nanofilms (**Figures S21**) pointed to an n-type behavior at room temperature as determined by the negative slope of the Hall resistance with respect to the magnetic field ($\mu_0 H$). Using the Hall signal, we estimated a charge mobility of 4.65 $cm^2/V{\cdot}s$ and a charge carrier density of $4.4{\cdot}10^{19}$ cm^{-3} at 30 °C (**Figure 4d**). This mobility is somewhat lower than the value originally reported for a Cu-BHT field-effect transistor (FET).[44] However, recent studies have highlighted the tendency to overestimate field-effect mobilities in FET devices with non-ideal characteristics.[55,56] The transfer characteristic of our CVD Cu BHT top-gated FET devices shows no clear field effect, suggesting a metallic behavior (**Figure S22**).[6] Nevertheless, the high-quality fabrication of the Hall bar structure combined with the Zero-Offset Hall characterization method allowed a reduced offset of the Hall resistance data, which avoided the additional data treatment otherwise required for geometrically non-homogenous Hall bar structures. In addition, through the fabrication of these devices, we demonstrated the compatibility of our CVD method with microscale patterning of integrated devices, thus placing our technology closer to the integration of metal-organic materials in microelectronics.

CONCLUSION

In conclusion, we have shown a novel CVD procedure for the preparation of high-quality, oriented Cu-BHT nanofilms with a well-controlled thickness through the solid-vapor conversion of a CuO precursor layer. Furthermore, our CVD method enables high-fidelity patterning of features down to 1 μm, without the risk of etchant damage to the Cu-BHT layer. This approach facilitates the fabrication of well-defined, micrometric Hall bar devices that were used to accurately measure the conductivity parameters. The demonstrated deposition and patterning fabrication flow showcases the advantages of vapor-phase methods and brings the integration of metal-organic nanofilms into microelectronic devices closer.

ASSOCIATED CONTENT

Supporting Information. Experimental procedures and additional characterization. Figures S1-22 and Table S1. This material is available free of charge via the Internet at http://pubs.acs.org.

AUTHOR INFORMATION

Corresponding Author

Víctor Rubio-Giménez - *Centre for Membrane Separations, Adsorption, Catalysis and Spectroscopy (cMACS), Katholieke Universiteit Leuven, Celestijnenlaan 200F, 3001 Leuven, Belgium*
Email: victorrubio.gimenez@kuleuven.be

Rob Ameloot - *Centre for Membrane Separations, Adsorption, Catalysis and Spectroscopy (cMACS), Katholieke Universiteit Leuven, Celestijnenlaan 200F, 3001 Leuven, Belgium*
Email: rob.ameloot@kuleuven.be

Author Contributions

The manuscript was written through contributions of all authors. All authors have given approval to the final version of the manuscript.

Notes

The authors declare no competing financial interest.

ACKNOWLEDGMENT

This project has received funding from the European Union's Horizon 2020 research and innovation program under the FETOPEN-1-2016-2017 grant agreement no 801464 (project acronym: SPRINT). R.A. and R.D. acknowledge the financial support from the European Research Council (ERC) under grant agreements no 716472 (VAPORE) and 852909 (FC2DMOF), respectively. R.A. thanks the Research Foundation Flanders (FWO Vlaanderen) for projects G083016N, G0E6319N and G087422N, and KU Leuven for project C14/20/085. R.D. acknowledges the funding from the German Research Foundation (DFG) for projects SPP1928, COORNET and CRC1415 (No. 417590517). V.R.-G. acknowledges FWO Vlaanderen for a Marie Skłodowska Curie Actions-Seal of Excellence and a Junior Postdoctoral Fellowship (12Z6520N and 1263622N, respectively). M.L.T. acknowledges FWO Vlaanderen for a senior postdoctoral fellowship (12ZK720N). D.E.K. acknowledges the Marie Sklodowska Curie Training Network HYCOAT (grant agreement 765378) and a KU Leuven Postdoctoral Mandate (PDMT2/21/057) for the financial support. G.A. and J.S. thank FWO Vlaanderen for their PhD fellowships (1SA7320N and 1H8123N, respectively). We thank Miriam Candelaria Rodríguez González for her assistance in using the AFM and Zichao Li for the electrical conductivity measurements. The authors are also grateful to Paul Van der Aerschot, Bart Leclercq, César Parra-Cabrera and Annelies Vanvlasselaer for their technical support. We thank Silvia Armini, Philippe Vereecken and Imec for access to the thermal evaporation equipment. We acknowledge Elettra Sincrotrone Trieste for providing access to its synchrotron radiation facilities (proposal 20210060) and thank Luisa Barba and Nicola Demitri for their assistance using beamline XRD1. We acknowledge DESY (Hamburg, Germany), a member of the Helmholtz Association HGF, for the provision of experimental facilities. Parts of this research were carried out at PETRA III and we would like to thank for assistance in using P23. Beamtime was allocated for proposals I-20200183 and I-20211632. The research leading to this result has been supported by the project CALIPSOplus under Grant Agreement 730872 from the EU Framework Programme for Research and Innovation HORIZON 2020.

REFERENCES

(1) Ko, M.; Mendecki, L.; Mirica, K. A. Conductive Two-Dimensional Metal-Organic Frameworks as Multifunctional Materials. *Chem. Commun.* **2018**, *54* (57), 7873–7891. https://doi.org/10.1039/C8CC02871K.

(2) Allendorf, M. D.; Dong, R.; Feng, X.; Kaskel, S.; Matoga, D.; Stavila, V. Electronic Devices Using Open Framework Materials. *Chem. Rev.* **2020**, *120* (16), 8581–8640. https://doi.org/10.1021/acs.chemrev.0c00033.

(3) Wang, M.; Dong, R.; Feng, X. Two-Dimensional Conjugated Metal–Organic Frameworks (2D c-MOFs): Chemistry and Function for MOFtronics. *Chem. Soc. Rev.* **2021**, *50* (4), 2764–2793. https://doi.org/10.1039/D0CS01160F.

(4) Liu, J.; Chen, Y.; Feng, X.; Dong, R. Conductive 2D Conjugated Metal–Organic Framework Thin Films: Synthesis and Functions for (Opto-)Electronics. *Small Struct.* **2022**, *3* (5), 2100210. https://doi.org/10.1002/sstr.202100210.

(5) Zhang, X.; Zhou, Y.; Cui, B.; Zhao, M.; Liu, F. Theoretical Discovery of a Superconducting Two-Dimensional Metal-Organic Framework. *Nano Lett.* **2017**, *17* (10), 6166–6170. https://doi.org/10.1021/acs.nanolett.7b02795.

(6) Huang, X.; Zhang, S.; Liu, L.; Yu, L.; Chen, G.; Xu, W.; Zhu, D. Superconductivity in a Copper(II)-Based Coordination Polymer with Perfect Kagome Structure. *Angew. Chem. Int. Ed.* **2018**, *57* (1), 146–150. https://doi.org/10.1002/anie.201707568.

(7) Gao, J.; Geng, S.; Chen, Y.; Cheng, P.; Zhang, Z. Theoretical Exploration and Electronic Applications of Conductive Two-Dimensional Metal–Organic Frameworks. *Topics in Current Chemistry* **2020**, *378* (2), 25. https://doi.org/10.1007/s41061-020-0288-6.

(8) Yao, M.-S.; Lv, X.-J.; Fu, Z.-H.; Li, W.-H.; Deng, W.-H.; Wu, G.-D.; Xu, G. Layer-by-Layer Assembled Conductive Metal-Organic Framework Nanofilms for Room-Temperature Chemiresistive Sensing. *Angew. Chem. Int. Ed.* **2017**, *56* (52), 16510–16514. https://doi.org/10.1002/anie.201709558.

(9) Rubio-Giménez, V.; Almora-Barrios, N.; Escorcia-Ariza, G.; Galbiati, M.; Sessolo, M.; Tatay, S.; Martí-Gastaldo, C. Origin of the Chemiresistive Response of Ultrathin Films of Conductive Metal-Organic Frameworks. *Angew. Chem. Int. Ed.* **2018**, *57* (46), 15086–15090. https://doi.org/10.1002/anie.201808242.

(10) Yao, M.-S.; Zheng, J.-J.; Wu, A.-Q.; Xu, G.; Nagarkar, S. S.; Zhang, G.; Tsujimoto, M.; Sakaki, S.; Horike, S.; Otake, K.; Kitagawa, S. A Dual-Ligand Porous Coordination Polymer Chemiresistor with Modulated Conductivity and Porosity. *Angew. Chem. Int. Ed.* **2020**, *59* (1), 172–176. https://doi.org/10.1002/anie.201909096.

(11) Wu, G.; Huang, J.; Zang, Y.; He, J.; Xu, G. Porous Field-Effect Transistors Based on a Semiconductive Metal-Organic Framework. *J. Am. Chem. Soc.* **2017**, *139* (4), 1360–1363. https://doi.org/10.1021/jacs.6b08511.

(12) Ohata, T.; Nomoto, A.; Watanabe, T.; Hirosawa, I.; Makita, T.; Takeya, J.; Makiura, R. Uniaxially Oriented Electrically Conductive Metal–Organic Framework Nanosheets Assembled at Air/Liquid Interfaces. *ACS Appl. Mater. Interfaces* **2021**, *13* (45), 54570–54578. https://doi.org/10.1021/acsami.1c16180.

(13) Arora, H.; Dong, R.; Venanzi, T.; Zscharschuch, J.; Schneider, H.; Helm, M.; Feng, X.; Cánovas, E.; Erbe, A. Demonstration of a Broadband Photodetector Based on a Two-Dimensional Metal–Organic Framework. *Adv. Mater.* **2020**, *32* (9), 1907063. https://doi.org/10.1002/adma.201907063.

(14) Song, X.; Wang, X.; Li, Y.; Zheng, C.; Zhang, B.; Di, C.; Li, F.; Jin, C.; Mi, W.; Chen, L.; Hu, W. 2D Semiconducting Metal–Organic Framework Thin Films for Organic Spin Valves. *Angew. Chem. Int. Ed.* **2020**, *59* (3), 1118–1123. https://doi.org/10.1002/anie.201911543.

(15) Jin, Z.; Yan, J.; Huang, X.; Xu, W.; Yang, S.; Zhu, D.; Wang, J. Solution-Processed Transparent Coordination Polymer Electrode for Photovoltaic Solar Cells. *Nano Energy* **2017**, *40*, 376–381. https://doi.org/10.1016/j.nanoen.2017.08.028.

(16) Liu, J.; Song, X.; Zhang, T.; Liu, S.; Wen, H.; Chen, L. 2D Conductive Metal–Organic Frameworks: An Emerging Platform for Electrochemical Energy Storage. *Angew. Chem. Int. Ed.* **2021**, *60* (11), 5612–5624. https://doi.org/10.1002/anie.202006102.

(17) Falcaro, P.; Ricco, R.; Doherty, C. M.; Liang, K.; Hill, A. J.; Styles, M. J. MOF Positioning Technology and Device Fabrication. *Chem. Soc. Rev.* **2014**, *43*, 5513–5560. https://doi.org/10.1039/C4CS00089G.

(18) Ruiz-Zambrana, C. L.; Malankowska, M.; Coronas, J. Metal Organic Framework Top-down and Bottom-up Patterning Techniques. *Dalton Trans.* **2020**, *49* (43), 15139–15148. https://doi.org/10.1039/D0DT02207A.

(19) Stassen, I.; Burtch, N.; Talin, A.; Falcaro, P.; Allendorf, M.; Ameloot, R. An Updated Roadmap for the Integration of Metal-Organic Frameworks with Electronic Devices and Chemical Sensors. *Chem. Soc. Rev.* **2017**, *46* (11), 3185–3241. https://doi.org/10.1039/C7CS00122C.

(20) Rubio-Giménez, V.; Tatay, S.; Martí-Gastaldo, C. Electrical Conductivity and Magnetic Bistability in Metal–Organic Frameworks and Coordination Polymers: Charge Transport and Spin Crossover at the Nanoscale. *Chem. Soc. Rev.* **2020**, *49* (15), 5601–5638. https://doi.org/10.1039/C9CS00594C.

(21) Stassen, I.; De Vos, D.; Ameloot, R. Vapor-Phase Deposition and Modification of Metal-Organic Frameworks: State-of-the-Art and Future Directions. *Chem. Eur. J.* **2016**, *22* (41), 14452–14460. https://doi.org/10.1002/chem.201601921.

(22) Su, P.; Tu, M.; Ameloot, R.; Li, W. Vapor-Phase Processing of Metal–Organic Frameworks. *Acc. Chem. Res.* **2022**, *55* (2), 186–196. https://doi.org/10.1021/acs.accounts.1c00600.

(23) Stassen, I.; Styles, M.; Grenci, G.; Gorp, H. V.; Vanderlinden, W.; Feyter, S. D.; Falcaro, P.; Vos, D. D.; Vereecken, P.; Ameloot, R. Chemical Vapour Deposition of Zeolitic Imidazolate Framework Thin Films. *Nat. Mater.* **2016**, *15* (3), 304–310.

(24) Ma, X.; Kumar, P.; Mittal, N.; Khlyustova, A.; Daoutidis, P.; Mkhoyan, K. A.; Tsapatsis, M. Zeolitic Imidazolate Framework Membranes Made by Ligand-Induced Permselectivation. *Science* **2018**, *361* (6406), 1008–1011. https://doi.org/10.1126/science.aat4123.

(25) Krishtab, M.; Stassen, I.; Stassin, T.; Cruz, A. J.; Okudur, O. O.; Armini, S.; Wilson, C.; De Gendt, S.; Ameloot, R. Vapor-Deposited Zeolitic Imidazolate Frameworks as Gap-Filling Ultra-Low-k Dielectrics. *Nat. Commun.* **2019**, *10* (1), 3729. https://doi.org/10.1038/s41467-019-11703-x.

(26) Cruz, A. J.; Stassen, I.; Krishtab, M.; Marcoen, K.; Stassin, T.; Rodríguez-Hermida, S.; Teyssandier, J.; Pletincx, S.; Verbeke, R.; Rubio-Giménez, V.; Tatay, S.; Martí-Gastaldo, C.; Meersschaut, J.; Vereecken, P. M.; De Feyter, S.; Hauffman, T.; Ameloot, R. Integrated Cleanroom Process for the Vapor-Phase Deposition of Large-Area Zeolitic Imidazolate Framework Thin Films. *Chem. Mater.* **2019**, *31* (22), 9462–9471. https://doi.org/10.1021/acs.chemmater.9b03435.

(27) Huang, J.-K.; Saito, N.; Cai, Y.; Wan, Y.; Cheng, C.-C.; Li, M.; Shi, J.; Tamada, K.; Tung, V. C.; Li, S.; Li, L.-J. Steam-Assisted Chemical Vapor Deposition of Zeolitic Imidazolate Framework. *ACS Materials Lett.* **2020**, *2* (5), 485–491. https://doi.org/10.1021/acsmaterialslett.0c00026.

(28) Tu, M.; Kravchenko, D. E.; Xia, B.; Rubio-Giménez, V.; Wauteraerts, N.; Verbeke, R.; Vankelecom, I. F. J.; Stassin, T.; Egger, W.; Dickmann, M.; Amenitsch, H.; Ameloot, R. Template-Mediated Control over Polymorphism in the Vapor-Assisted Formation of Zeolitic Imidazolate Framework Powders and Films. *Angew. Chem. Int. Ed.* **2021**, *60* (14), 7553–7558. https://doi.org/10.1002/anie.202014791.

(29) Miao, Y.; Lee, D. T.; de Mello, M. D.; Ahmad, M.; Abdel-Rahman, M. K.; Eckhert, P. M.; Boscoboinik, J. A.; Fairbrother, D. H.; Tsapatsis, M. Solvent-Free Bottom-up Patterning of Zeolitic Imidazolate Frameworks. *Nat. Commun.* **2022**, *13* (1), 420. https://doi.org/10.1038/s41467-022-28050-z.

(30) Tietze, M. L.; Obst, M.; Arnauts, G.; Wauteraerts, N.; Rodríguez-Hermida, S.; Ameloot, R. Parts-per-Million Detection of Volatile Organic Compounds via Surface Plasmon Polaritons and Nanometer-Thick Metal–Organic Framework Films. *ACS Appl. Nano Mater.* **2022**, *5* (4), 5006–5016. https://doi.org/10.1021/acsanm.2c00012.

(31) Medishetty, R.; Zhang, Z.; Sadlo, A.; Cwik, S.; Peeters, D.; Henke, S.; Mangayarkarasi, N.; Devi, A. Fabrication of Zinc-Dicarboxylate- and Zinc-Pyrazolate-Carboxylate-Framework Thin Films through Vapour-Solid Deposition. *Dalton Trans.* **2018**, *47* (40), 14179–14183. https://doi.org/10.1039/C8DT00352A.

(32) Stassin, T.; Rodríguez-Hemida, S.; Schrode, B.; Cruz, A. J.; Carraro, F.; Kravchenko, D.; Creemers, V.; Stassen, I.; Hauffman, T.; De Vos, D. E.; Falcaro, P.; Resel, R.; Ameloot, R. Vapour-Phase Deposition of Oriented Copper Dicarboxylate Metal-Organic Framework Thin Films. *Chem. Commun.* **2019**, *55*, 10056–10059. https://doi.org/10.1039/C9CC05161A.

(33) Stassin, T.; Stassen, I.; Marreiros, J.; Cruz, A. J.; Verbeke, R.; Tu, M.; Reinsch, H.; Dickmann, M.; Egger, W.; Vankelecom, I. F. J.; De Vos, D. E.; Ameloot, R. Solvent-Free Powder Synthesis and MOF-CVD Thin Films of the Large-Pore Metal–Organic Framework MAF-6. *Chem. Mater.* **2020**, *32* (5), 1784–1793. https://doi.org/10.1021/acs.chemmater.9b03807.

(34) Stassin, T.; Stassen, I.; Wauteraerts, N.; Cruz, A. J.; Kräuter, M.; Coclite, A. M.; De Vos, D.; Ameloot, R. Solvent-Free Powder Synthesis and Thin Film Chemical Vapor Deposition of a Zinc Bipyridyl-Triazolate Framework. *Eur. J. Inorg. Chem.* **2020**, *2020* (1), 71–74. https://doi.org/10.1002/ejic.201901051.

(35) Kravchenko, D. E.; Cruz, A. J.; Rodríguez-Hermida, S.; Wauteraerts, N.; Hauffman, T.; Ameloot, R. Templated Solvent-Free Powder Synthesis and MOF-CVD Films of the Ultramicroporous Metal–Organic Framework α-Magnesium Formate. *Chem. Mater.* **2020**, *32* (24), 10469–10475. https://doi.org/10.1021/acs.chemmater.0c03212.

(36) Claire, F. J.; Solomos, M. A.; Kim, J.; Wang, G.; Siegler, M. A.; Crommie, M. F.; Kempa, T. J. Structural and Electronic Switching of a Single Crystal 2D Metal-Organic Framework Prepared by Chemical Vapor Deposition. *Nat. Commun.* **2020**, *11* (1), 5524. https://doi.org/10.1038/s41467-020-19220-y.

(37) Ogle, J.; Lahiri, N.; Jaye, C.; Tassone, C. J.; Fischer, D. A.; Louie, J.; Whittaker-Brooks, L. Semiconducting to Metallic Electronic Landscapes in Defects-Controlled 2D π-d Conjugated Coordination Polymer Thin Films. *Adv. Funct. Mater.* **2021**, *31* (4), 2006920. https://doi.org/10.1002/adfm.202006920.

(38) Choe, M.; Koo, J. Y.; Park, I.; Ohtsu, H.; Shim, J. H.; Choi, H. C.; Park, S. S. Chemical Vapor Deposition of Edge-on Oriented 2D Conductive Metal–Organic Framework Thin Films. *J. Am. Chem. Soc.* **2022**, *144* (37), 16726–16731. https://doi.org/10.1021/jacs.2c07135.

(39) Rodríguez-Hermida, S.; Kravchenko, D. E.; Wauteraerts, N.; Ameloot, R. Vapor-Assisted Powder Synthesis and Oriented MOF-CVD Thin Films of the Metal–Organic Framework HKUST-1. *Inorg. Chem.* **2022**, *61* (45), 17927–17931. https://doi.org/10.1021/acs.inorgchem.2c02490.

(40) Liu, J.; Woll, C. Surface-Supported Metal-Organic Framework Thin Films: Fabrication Methods, Applications, and Challenges. *Chem. Soc. Rev.* **2017**, *46*, 5730–5770. https://doi.org/10.1039/C7CS00315C.

(41) Dong, R.; Han, P.; Arora, H.; Ballabio, M.; Karakus, M.; Zhang, Z.; Shekhar, C.; Adler, P.; Petkov, P. St.; Erbe, A.; Mannsfeld, S. C. B.; Felser, C.; Heine, T.; Bonn, M.; Feng, X.; Cánovas, E. High-Mobility Band-like Charge Transport in a Semiconducting Two-Dimensional Metal-Organic Framework. *Nat. Mater.* **2018**, *17*, 1027–1032. https://doi.org/10.1038/s41563-018-0189-z.

(42) Tu, M.; Xia, B.; Kravchenko, D. E.; Tietze, M. L.; Cruz, A. J.; Stassen, I.; Hauffman, T.; Teyssandier, J.; De Feyter, S.; Wang, Z.; Fischer, R. A.; Marmiroli, B.; Amenitsch, H.; Torvisco, A.; Velásquez-Hernández, M. de J.; Falcaro, P.; Ameloot, R. Direct X-Ray and Electron-Beam Lithography of Halogenated Zeolitic Imidazolate Frameworks. *Nat. Mater.* **2021**, *20* (1), 93–99. https://doi.org/10.1038/s41563-020-00827-x.

(43) Xie, L. S.; Skorupskii, G.; Dincă, M. Electrically Conductive Metal–Organic Frameworks. *Chem. Rev.* **2020**, *120* (16), 8536–8580. https://doi.org/10.1021/acs.chemrev.9b00766.

(44) Huang, X.; Sheng, P.; Tu, Z.; Zhang, F.; Wang, J.; Geng, H.; Zou, Y.; Di, C.; Yi, Y.; Sun, Y.; Xu, W.; Zhu, D. A Two-Dimensional $[$pi$]$-d Conjugated Coordination Polymer with Extremely High Electrical Conductivity and Ambipolar Transport Behaviour. *Nat. Commun.* **2015**, *6*, 7408.

(45) Chen, X.; Lu, Y.; Dong, J.; Ma, L.; Yi, Z.; Wang, Y.; Wang, L.; Wang, S.; Zhao, Y.; Huang, J.; Liu, Y. Ultrafast In Situ Synthesis of Large-Area Conductive Metal–Organic Frameworks on Substrates for Flexible Chemiresistive Sensing. *ACS Appl. Mater. Interfaces* **2020**, *12* (51), 57235–57244. https://doi.org/10.1021/acsami.0c18422.

(46) Regoutz, A.; Mascheck, M.; Wiell, T.; Eriksson, S. K.; Liljenberg, C.; Tetzner, K.; Williamson, B. A. D.; Scanlon, D. O.; Palmgren, P. A Novel Laboratory-Based Hard X-Ray Photoelectron Spectroscopy System. *Rev. Sci. Instrum.* **2018**, *89* (7), 073105. https://doi.org/10.1063/1.5039829.

(47) Wang, L.; Chen, X.; Yi, Z.; Xu, R.; Dong, J.; Wang, S.; Zhao, Y.; Liu, Y. Facile Synthesis of Conductive Metal–Organic Frameworks Nanotubes for Ultrahigh-Performance Flexible NO Sensors. *Small Methods* **2022**, *6* (9), 2200581. https://doi.org/10.1002/smtd.202200581.

(48) Sung, M. M.; Sung, K.; Kim, C. G.; Lee, S. S.; Kim, Y. Self-Assembled Monolayers of Alkanethiols on Oxidized Copper Surfaces. *J. Phys. Chem. B* **2000**, *104* (10), 2273–2277. https://doi.org/10.1021/jp992995h.

(49) Bergsman, D. S.; Liu, T.-L.; Closser, R. G.; Nardi, K. L.; Draeger, N.; Hausmann, D. M.; Bent, S. F. Formation and Ripening of Self-Assembled Multilayers from the Vapor-Phase Deposition of Dodecanethiol on Copper Oxide. *Chem. Mater.* **2018**, *30* (16), 5694–5703. https://doi.org/10.1021/acs.chemmater.8b02150.

(50) Laibinis, P. E.; Whitesides, G. M.; Allara, D. L.; Tao, Y. T.; Parikh, A. N.; Nuzzo, R. G. Comparison of the Structures and Wetting Properties of Self-Assembled Monolayers of n-Alkanethiols on the Coinage Metal Surfaces, Copper, Silver, and Gold. *J. Am. Chem. Soc.* **1991**, *113* (19), 7152–7167. https://doi.org/10.1021/ja00019a011.

(51) Beccari, M.; Kanjilal, A.; Betti, M. G.; Mariani, C.; Floreano, L.; Cossaro, A.; Di Castro, V. Characterization of Benzenethiolate Self-Assembled Monolayer on Cu(100) by XPS and NEXAFS. *J. Electron. Spectros. Relat. Phenomena* **2009**, *172* (1), 64–68. https://doi.org/10.1016/j.elspec.2009.03.004.

(52) Huang, X.; Yao, H.; Cui, Y.; Hao, W.; Zhu, J.; Xu, W.; Zhu, D. Conductive Copper Benzenehexathiol Coordination Polymer as a Hydrogen Evolution Catalyst. *ACS Appl. Mater. Interfaces* **2017**, *9* (46), 40752–40759. https://doi.org/10.1021/acsami.7b14523.

(53) Wu, Z.; Adekoya, D.; Huang, X.; Kiefel, M. J.; Xie, J.; Xu, W.; Zhang, Q.; Zhu, D.; Zhang, S. Highly Conductive Two-Dimensional Metal–Organic Frameworks for Resilient Lithium Storage with Superb Rate Capability. *ACS Nano* **2020**, *14* (9), 12016–12026. https://doi.org/10.1021/acsnano.0c05200.

(54) Givaja, G.; Amo-Ochoa, P.; Gomez-Garcia, C. J.; Zamora, F. Electrical Conductive Coordination Polymers. *Chem. Soc. Rev.* **2012**, *41* (1), 115–147. https://doi.org/10.1039/C1CS15092H.

(55) Bittle, E. G.; Basham, J. I.; Jackson, T. N.; Jurchescu, O. D.; Gundlach, D. J. Mobility Overestimation Due to Gated Contacts in Organic Field-Effect Transistors. *Nat. Commun.* **2016**, *7* (1), 10908. https://doi.org/10.1038/ncomms10908.

(56) Aubrey, M. L.; Wiers, B. M.; Andrews, S. C.; Sakurai, T.; Reyes-Lillo, S. E.; Hamed, S. M.; Yu, C.-J.; Darago, L. E.; Mason, J. A.; Baeg, J.-O.; Grandjean, F.; Long, G. J.; Seki, S.; Neaton, J. B.; Yang, P.; Long, J. R. Electron Delocalization and Charge Mobility as a Function of Reduction in a Metal-Organic Framework. *Nat. Mater.* **2018**, *17* (7), 625–632. https://doi.org/10.1038/s41563-018-0098-1.